BULLETIN OF THE POLISH ACADEMY OF SCIENCES
TECHNICAL SCIENCES, Vol. 72(2), 2024, Article number: e148873
DOI: 10.24425/bpasts.2024.148873



# Mesh suitability for CFD simulations performed on axial compressor airfoil cascades

**Adam TATER*, Pavel MAČÁK, and Patrik KOVÁŘ**

Center of Aviation and Space Research, Faculty of Mechanical Engineering, Czech Technical University in Prague, Jugoslávských partyzánů 1580/3, 16000, Prague 6, Czech Republic

**Abstract.** In the presented paper, two different meshing strategies are compared to show the accuracy advantage of properly constructed mesh. For this purpose, it was necessary to automatize simulation process, in order to perform a number of calculations without the necessity of user interaction. Later, a method of results extrapolation as well as a way of judging mesh quality are introduced for more throughout comparison of presented discretization strategies. The latter method, called grid convergence index, is also used to calculate probability range of accurate result. To conclude, outcomes of this study are in agreement with general opinon on pracitces for an accurate CFD result. Structured O-type mesh with refinement at wall boundaries (often referred to as "inflation layers") performs better than simple free mesh.

**Keywords:** automation; axial compressor cascade; CFD; grid convergence index; Richardson extrapolation.

## 1. INTRODUCTION

Axial compressor consists of discs with rotor blades and rings with vanes of stator. In contrast with radial-flow compressors it has lower pressure ratio per single stage but higher efficiency. The next advantage of axial-flow compressors is their small frontal area at higher mass flow rates [1]. Axial compressors rotor and stator blades are created with a set of airfoils that are constructed radially on top of each other. A way to quantify performance of designed blading is testing of the airfoil cascade in a wind tunnel, as in [2] or [3]. Due to lower time and financial requirements computational fluid dynamics (CFD), especially applied on planar 2D problems, looks like a faster and cheaper way to investigate performance of designed airfoil profiles.

Accuracy of simulation results from CFD is an important and often discussed topic. Simulation of turbulent, compressible and viscous flow is a very common situation in engineering applications. Step one of every simulation is the computational domain discretization, which plays an essential role in achieving accurate results. Due to this, methods for mesh suitability investigation were developed and many of those are mentioned in [4]. One of the methods for judging mesh quality is the Richardson's extrapolation followed by calculation of the grid convergence index (GCI). Consequently, a range with reliable chance of containing accurate solution is set. This procedure was applied in many different applications [5–8].

In this paper, automatized computational CFD tool based on Navier-Stokes equations for predicting airfoil cascade losses is presented. Several simulations are performed on hybrid and free meshes. Mesh suitability is investigated using Richardson extrapolation. Discretization errors resulting from using different mesh sizes and reliability of results are estimated via GCI. Last paragraph should outline the paper organization, with the contents of sections and conclusions.

## 2. GOVERNING EQUATIONS

This section discusses the governing equations used in consequent CFD simulations.

### 2.1. Navier-Stokes equations

The most general system of equations modeling turbulent, compressible and viscous flow are the Navier-Stokes equations, defined in [9]. They are composed of mass, momentum and energy conservation laws respectively written as

$$\frac{\partial \rho}{\partial t} + \nabla \cdot (\rho \boldsymbol{u}) = 0, \tag{1}$$

$$\frac{\partial \rho \boldsymbol{u}}{\partial t} + \nabla \cdot (\rho \boldsymbol{u} \otimes \boldsymbol{u}) + \nabla p = \rho \boldsymbol{f} + \nabla \cdot \boldsymbol{\tau}, \tag{2}$$

$$\frac{\partial e}{\partial t} + \nabla \cdot ((e+p)\boldsymbol{u}) = \nabla \cdot (\boldsymbol{\tau} \cdot \boldsymbol{u}) - \nabla \cdot \boldsymbol{q} + Q, \tag{3}$$

where $\boldsymbol{\tau}$ is the shear stress tensor, $\boldsymbol{f}$ is the force per unit of mass vector, $Q$ is transferred heat per unit of volume. $e$ is the total energy per unit volume, defined as $e = \rho E$, where $E$ is the sum of internal and kinetic energy.

Solving Navier-Stokes equations in aforementioned form leads to direct numerical simulation (DNS). For DNS the computation mesh has to resolve scales from the characteristic length of airfoil up to Kolmogorov's microscales [10]. This is unsatisfying for engineering purposes, because number of operations

*e-mail: adam.tater@fs.cvut.cz

Manuscript submitted 2022-04-15, revised 2023-12-14, initially accepted for publication 2023-12-14, published in March 2024.

required to complete such simulation grows rapidly (proportionally to $\approx \mathrm{Re}^{9/4}$). Fortunately, there are models, described in [11] and [12], based on decomposition of instantaneous variables to averaged part and fluctuating part.

### 2.2. Favre averaged Navier-Stokes equations

There are two types of averaging, Reynolds averaging for density and pressure

$$\overline{\phi} = \lim_{T\to\infty} \frac{1}{T} \int_{t}^{t+T} \phi(\tau)\,\mathrm{d}\tau, \tag{4}$$

$$\phi = \overline{\phi} + \phi', \tag{5}$$

and Favre averaging for remaining variables

$$\tilde{\phi} = \frac{1}{\overline{\rho}} \lim_{T\to\infty} \frac{1}{T} \int_{t}^{t+T} \rho(\tau)\phi(\tau)\,\mathrm{d}\tau, \tag{6}$$

$$\phi = \tilde{\phi} + \phi'', \tag{7}$$

where $\phi$ is instantaneous variable and $\phi'$, $\phi''$ are fluctuating parts. By substituting these decomposed variables into equations (1), (2) and (3), we obtain Favre averaged Navier-Stokes equations. Conservation laws can be then rewritten using Einstein notation as

$$\frac{\partial \overline{\rho}}{\partial t} + \frac{\partial(\overline{\rho}\tilde{u}_i)}{\partial x_i} = 0, \tag{8}$$

$$\frac{\partial(\overline{\rho}\tilde{u}_i)}{\partial t} + \frac{\partial(\overline{\rho}\tilde{u}_i\tilde{u}_j)}{\partial x_j} + \frac{\partial \overline{p}}{\partial x_i} = \frac{\partial}{\partial x_j}\left(\overline{\tau_{ij}} - \overline{\rho u_i'' u_j''}\right), \tag{9}$$

$$\frac{\partial \tilde{e}}{\partial t} + \frac{\partial(\tilde{e}+\overline{p})\tilde{u}_j}{\partial x_j} = -\frac{\partial}{\partial x_j}\left(\bar{q}_j + \overline{\rho u_j'' h''} - \overline{\tau_{ij}'' u_i''} + \frac{1}{2}\overline{\rho u_j'' u_i'' u_i''}\right) + \frac{\partial}{\partial x_j}\left(\tilde{u}_i(\overline{\tau_{ij}} - \overline{\rho u_i'' u_j''})\right), \tag{10}$$

where $\overline{\tau_{ij}}$ is given by

$$\overline{\tau_{ij}} = 2\overline{\mu S_{ij}}, \quad \overline{\mu} = \mu_{\mathrm{ref}}\left(\frac{\rho_{\mathrm{ref}}\overline{p}}{p_{\mathrm{ref}}\overline{\rho}}\right)^{\frac{3}{4}}, \qquad \overline{S_{ij}} = \frac{1}{2}\left(\frac{\partial \tilde{u}_i}{\partial x_j} + \frac{\partial \tilde{u}_j}{\partial x_i} - \frac{2}{3}\delta_{ij}\frac{\partial \tilde{u}_k}{\partial x_k}\right), \tag{11}$$

and $\overline{q_j}$ is given by

$$\overline{q_j} = -\frac{\kappa\overline{\mu}}{(\kappa-1)\,\mathrm{Pr}}\left(\frac{\overline{p}}{\overline{\rho}}\right), \tag{12}$$

where Pr is Prandtl's number. In order to close this system of equations, calorically perfect gas model is assumed. By averaging the state equation we obtain

$$\overline{p} = (\kappa-1)\left(\tilde{e} - \frac{1}{2}\overline{\rho}\tilde{u}_j\tilde{u}_j - \overline{\rho}k\right), \quad k = \frac{1}{2}\overline{u_i'' u_i''}, \tag{13}$$

where $k$ is turbulent kinetic energy.

### 2.3. Transition SST turbulence model

In order to achieve the best results possible, 4-equation Transition SST turbulence model, sometimes known as $\gamma$-$\mathrm{Re}_\theta$ model first published in [13], was chosen. This model couples SST $k$-$\omega$ model equations, published in [14], with two other equations and tries to distinguish between laminar and turbulent regions of flow. The first added transport equation (18) is for intermittency $\gamma$ and the second equation (19) is for the transition onset criteria, in terms of fictive momentum-thickness Reynolds number $\widetilde{\mathrm{Re}}_{\theta t}$.

The transition model interacts with the SST $k$-$\omega$ model by modification of the $k$-equation as follows

$$\frac{\partial(\overline{\rho}k)}{\partial t} + \frac{\partial(\overline{\rho}k\tilde{u}_i)}{\partial x_i} = \frac{\partial}{\partial x_j}\left(\Gamma_k \frac{\partial k}{\partial x_j}\right) + G_k^\star - Y_k^\star, \tag{14}$$

$$Y_k^\star = \min\Big(\max(\gamma_{\mathrm{eff}}, 0.1), 1\Big)Y_k, \tag{15}$$

$$G_k^\star = \gamma_{\mathrm{eff}} G_k, \tag{16}$$

where $G_k$ and $Y_k$ are the original production and destruction terms from SST $k$-$\omega$ model and $\gamma_{\mathrm{eff}}$ can by found in [13]. The $\omega$-equation remains unchanged as

$$\frac{\partial(\overline{\rho}\omega)}{\partial t} + \frac{\partial(\overline{\rho}\omega\tilde{u}_i)}{\partial x_i} = \frac{\partial}{\partial x_j}\left(\Gamma_\omega \frac{\partial \omega}{\partial x_j}\right) + G_\omega - Y_\omega + D_\omega. \tag{17}$$

First equation defining the Transition model is the $\gamma$-equation, where $\gamma$ determines percentage of time the flow is turbulent or laminar, and is defined as

$$\frac{\partial(\overline{\rho}\gamma)}{\partial t} + \frac{\partial(\overline{\rho}\gamma\tilde{u}_i)}{\partial x_i} = \frac{\partial}{\partial x_j}\left(\left(\mu + \frac{\mu_t}{\sigma_\gamma}\right)\frac{\partial \gamma}{\partial x_j}\right) + P_{\gamma 1} - E_{\gamma 1} + P_{\gamma 2} - E_{\gamma 2}, \tag{18}$$

and the last equation forming the Transition SST model is $\widetilde{\mathrm{Re}}_{\theta t}$-equation, where $\widetilde{\mathrm{Re}}_{\theta t}$ is transition onset criteria expanded to the whole domain, and is defined as

$$\frac{\partial(\overline{\rho}\widetilde{\mathrm{Re}}_{\theta t})}{\partial t} + \frac{\partial(\overline{\rho}\widetilde{\mathrm{Re}}_{\theta t}\tilde{u}_i)}{\partial x_i} = \frac{\partial}{\partial x_j}\left(\sigma_{\theta t}\left(\mu + \mu_t\right)\frac{\partial \widetilde{\mathrm{Re}}_{\theta t}}{\partial x_j}\right) + P_{\theta t}. \tag{19}$$

All source terms in $\gamma$-equation and $\widetilde{\mathrm{Re}}_{\theta t}$-equation can be found in [13].

## 3. METHODOLOGY

This section discusses the methodology used in this paper.

### 3.1. Simulation process

In order to make a series of parametric calculations, in terms of changing airfoil geometry and using different boundary conditions, it is necessary to connect various applications and modules. The chosen approach is using a bash script to sequentially run different operations. Such script can be easily interpreted in Linux OS, which usually runs on servers, as well as in commonly used MS Windows (e.g. using MinGW console). For application in Section 4, following steps were automated and computational cycle with its vital components is visualized in Fig. 1.

1) run a Matlab script
   - *generate a set of airfoils and write coordinates into .csv files*
   - *create series of journal files for CFD simulation with required boundary conditions*
2) run ANSYS ICEM procedure
   - *generate mesh from previously created .csv files*
3) run ANSYS FLUENT procedure
   - *do CFD simulations and write .dat files*
4) run another Matlab script
   - *process the .dat files*

Alternatively, open-source software can be used to replace all these steps. C++ program instead of Matlab can be written to generate .csv and journal files in the first step. The same goes for post-processing part, where ParaView script can replace Matlab. Mesh can be created in Gmsh and CFD simulation can be performed by OpenFoam.

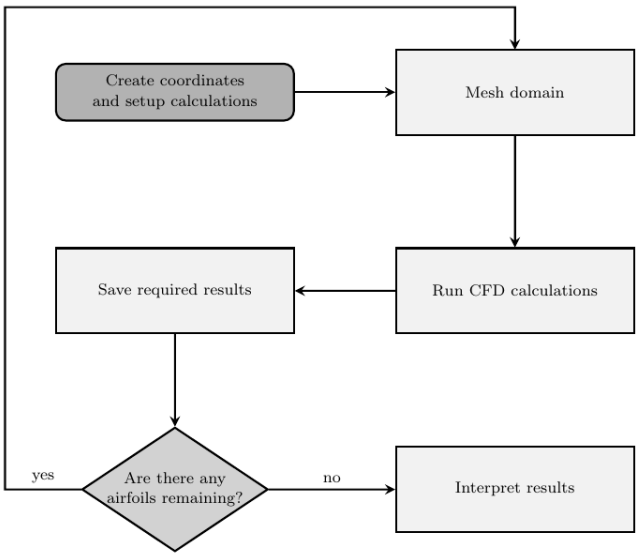


**Fig. 1.** Flowchart of the simulation process

### 3.2. Computational domain

The computational domain, shown in Fig. 2, consists of five curve segments and the volume limited by them. Upper and bottom boundaries are two equidistant lines, which are constructed from three segments. Those curves preserve their vertical distance on value $T$, which is a cascade parameter and says how far airfoils are from each other. The front segment is a line under the leading edge angle, followed by camber line of given profile. The back segment is then a line under the trailing edge angle. Left and right boundaries are vertical lines connecting upper and bottom edges, and finally the fifth curve is the airfoil placed in the middle.

### 3.3. Domain boundaries

During computational process the aforementioned curves are each assigned a boundary condition (BC). Upper and bottom boundaries are the periodic boundaries with translation periodicity in vertical direction. Left boundary is the inlet, right boundary is the outlet and the airfoil is the only wall boundary in this domain. This setup is sketched in Fig. 2.

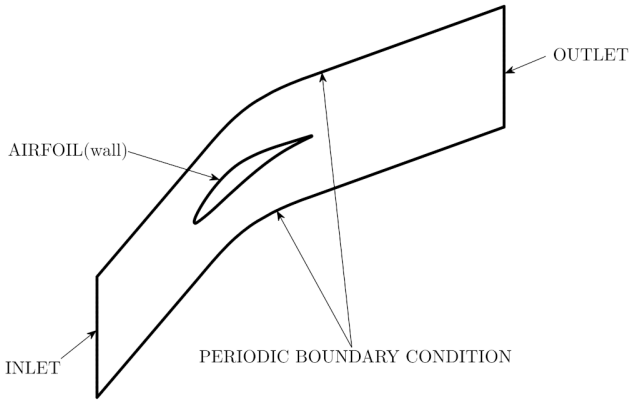


**Fig. 2.** Sketch of the computational domain with named boundaries

### 3.4. Mesh

Meshing airfoil cascades can prove to be much trickier task than meshing airfoils for external aerodynamics simulation, where C-type meshes are often the obvious choice as in [15]. Tight spacing in airfoil cascades does not give enough freedom for constructing structured mesh with low skewness. Meshing whole domain with structured grid can thus prove difficult, but is necessary only in most demanding cases. However, hybrid meshing strategy should surpass free mesh greatly for our purpose. When meshing an airfoil cascade, we work with coordinates of the profile itself as well as of profile camber line. Camberline proves useful, when creating curved part of periodic boundaries, as it is naturally in good agreement with resulting streamlines (at least for design inlet stream angle). Profile curve is used firstly to create the airfoil itself (wall boundary) and secondly to create an equidistant curve. This curve is then used to align structured part of the mesh, often referred to as O-mesh. The rest of the domain is then meshed freely, resulting in a hybrid mesh as already mentioned. The difference between simple free mesh and hybrid mesh can be seen in Fig. 3 and 4.

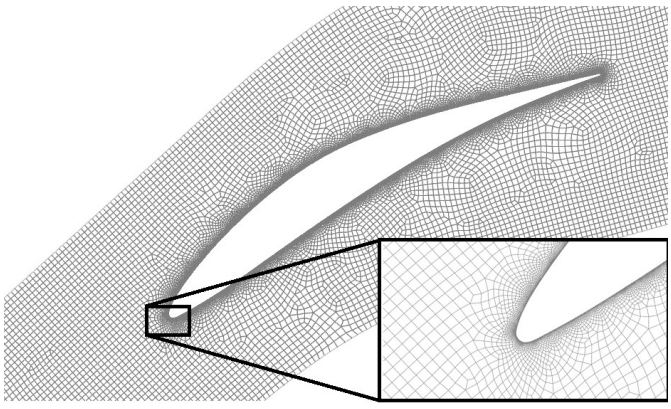

**Fig. 3.** Snapshot of the free mesh with zoom on the leading edge of the profile

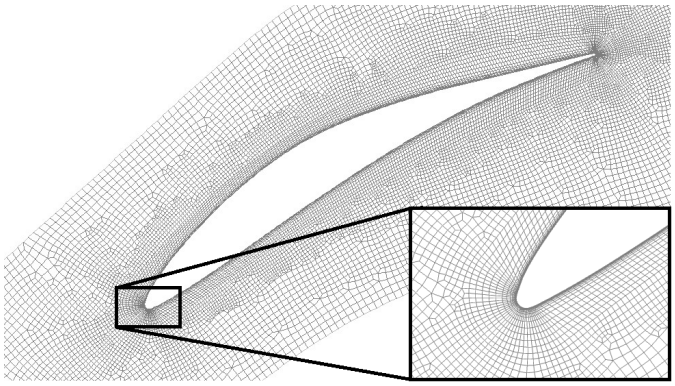

**Fig. 4.** Snapshot of the hybrid mesh with zoom on the leading edge of the profile

### 3.5. CFD simulation

Boundary conditions correspond to domain boundaries as described in subsection 3.3. Specifically, inlet is set as "*pressure inlet*", outlet as "*pressure outlet*" and wall is set as "*no-slip wall*". Simulated fluid is air with ideal gas material model. Effects of turbulence are modeled using Transition SST with *inlet intermittency* of 1, *turbulent intensity* 5 % and *turbulent viscosity ratio* 100. Considered atmospheric values are $p_{\text{atm}} = 101\,325$ Pa, $T_{\text{atm}} = 293.15$ K and the *specific heat ratio* $\kappa = 1.4$. Three variables are prescribed at inlet (*total pressure* $p_{\text{tot},1}$, *total temperature* $T_{\text{tot},1}$ and *angle of attack* $\alpha$) and one at outlet (*static pressure* $p_{\text{stat},2}$). *Total pressure at inlet* $p_{\text{tot},1}$ and *total temperature at inlet* $T_{\text{tot},1}$ are calculated as a function of *Mach number* $M$ using equations of gas dynamics, described in [9], for isentropic flow

$$p_{\text{tot}} = p_{\text{stat}} \left(1 + \frac{(\kappa-1)}{2} M^2\right)^{\frac{\kappa}{\kappa-1}}, \tag{20}$$

$$T_{\text{tot}} = T_{\text{stat}} \left(1 + \frac{(\kappa-1)}{2} M^2\right). \tag{21}$$

All simulations are planar and performed using finite volume method with theoretical second-order overall accuracy. Due to large differences in Mach numbers during various simulations, two different types of solvers are considered. For higher Mach numbers, implicit density-based solver with Roe-flux difference splitting is used, those methods are in general described in [16]. For lower Mach numbers, coupled pressure-based solver is used. Pressure-based solvers are in general described in [17], the coupled solver explicitly in [18].

## 4. RESULTS

In order to make the results trustworthy, this section is focused on comparison of numerical results with real measured data [2]. After that, mesh analysis is performed on different mesh types (free and hybrid) and length scales (coarse, medium and fine) in order to show hybrid mesh behaves better than free mesh.

### 4.1. Observed quantity

Quality of the mesh will be judged based on how well it predicts the total pressure loss coefficient $\Pi$, which is an important value used in compressor theory. It is defined in [2] as

$$\Pi = \frac{\overline{p_{\text{tot},1}} - \overline{p_{\text{tot},2}}}{\overline{p_{\text{tot},1}} - \overline{p_{\text{stat},1}}}. \tag{22}$$

Scalar values $p_{\text{tot},1}$, $p_{\text{stat},1}$ and $p_{\text{tot},2}$ are obtained as follows

$$\overline{p_{\text{tot},1}} = \int_{\text{inlet}} p_{\text{tot}}(x,y)\dot{m}(x,y)\,\mathrm{d}s, \tag{23}$$

$$\overline{p_{\text{stat},1}} = \int_{\text{inlet}} p_{\text{stat}}(x,y)\dot{m}(x,y)\,\mathrm{d}s, \tag{24}$$

$$\overline{p_{\text{tot},2}} = \int_{\text{outlet}} p_{\text{tot}}(x,y)\dot{m}(x,y)\,\mathrm{d}s, \tag{25}$$

where $p_{\text{tot}}$, $p_{\text{stat}}$ and mass flow $\dot{m}$ are scalar fields.

### 4.2. Validation task

The best validation of CFD calculation is comparison to experimental measurements. In this part a well-known case of MAN GHH 1-S1 airfoil cascade is computed and the results are confronted with measurements published in [2]. Total pressure loss coefficient $\Pi$ depending on Mach number and angle of attack is shown in Fig. 5a. Hereafter the simulation results for design conditions are displayed via Mach number isocurves throughout the cascade in Fig. 5b.

### 4.3. Richardson extrapolation

In order to possibly achieve more accurate results, Richardson extrapolation defined in [19] is used. It requires performing the same simulation on meshes of different scales $h$ and for this reason three meshes of each type were created by refining their scales by factor of two

$$r = \frac{h_2}{h_1} = \frac{h_3}{h_2} = 2, \tag{26}$$

where $r$ is mesh refinement ratio and numbers 3, 2 and 1 represent coarse, medium and fine scales respectively. Information on number of cells forming each mesh can be found in Table 1. Richardson extrapolation can be then used to extrapolate towards the exact solution.

**Table 1**
Number of cells forming different meshes

| Mesh Density | | Coarse | Medium | Fine |
|---|---|---|---|---|
| Number of cells | Free mesh | 105547 | 419356 | 1667689 |
| | Hybrid mesh | 107002 | 426826 | 1717147 |

Considering total pressure loss coefficient $\Pi$ as a dependent variable (i.e. a continuous and differentiable function of scale $h$) the numerical error can be expressed as

$$e_h = \Pi_{\text{exact}} - \Pi_h = C_1 h + C_2 h^2 + \ldots, \tag{27}$$

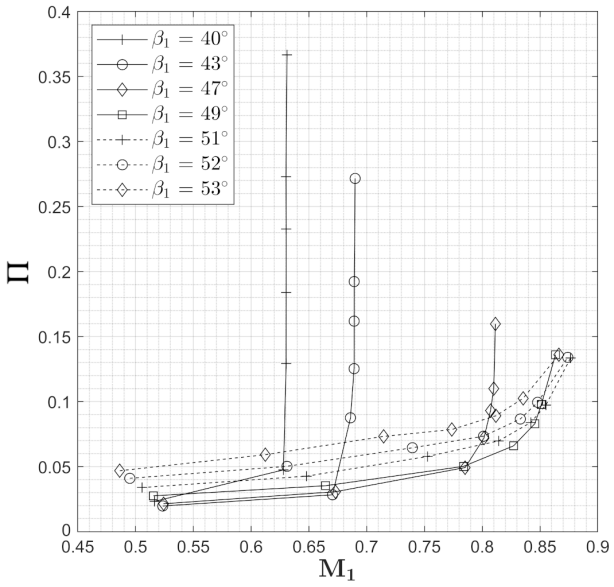


(a)

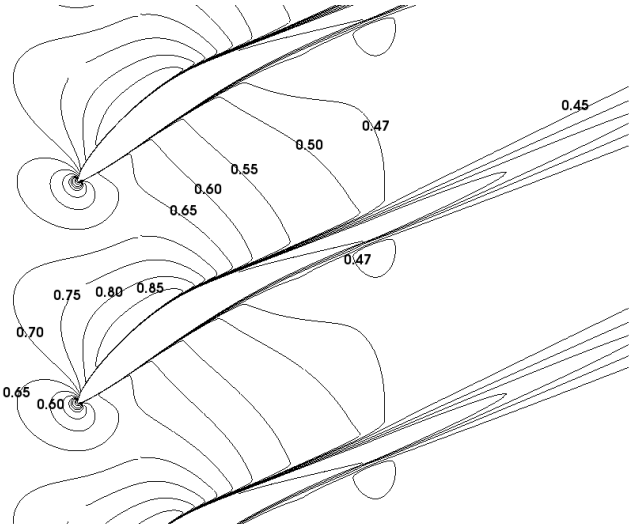


(b)

**Fig. 5.** Validation task. (a) Total pressure loss coefficient development depending on the angle of incidence; (b) Mach number isocurves through the cascade during design conditions

and for small values of $h$, terms with higher powers of $h$ can be omitted. After that, exact is replaced with ext to denote an extrapolated value and following equations are obtained

$$\Pi_{\text{ext}} - \Pi_i = C h_i^n, \quad i = \langle 1,3 \rangle \in \mathbb{N}, \tag{28}$$

where $C$ represents a coefficient that can be a function of the coordinates, but not of the mesh size and $n$ is the apparent order of the method. According to [19], the solution of the three previous equations for the three unknowns is

$$n = \frac{\ln\left(\dfrac{\Pi_2 - \Pi_3}{\Pi_1 - \Pi_2}\right)}{\ln(r)}, \quad \Pi_{\text{ext}} = \frac{2^n \Pi_1 - \Pi_2}{2^n - 1}, \quad C = \frac{\Pi_{\text{ext}} - \Pi_1}{h^n}. \tag{29}$$

Table 2 shows results of these simulations, namely the values of total pressure loss coefficient for different scales $h$ and from Richardson extrapolation $\Pi_{\text{ext}}$, and then the apparent order of the method $n$ as a function of Mach number at the inlet $M_1$.

From values of $\Pi$ in Table 2, it is apparent, that apart from cases of $M_1 = 0.48$ and $M_1 = 0.53$, asymptotic convergence of $\Pi$, which is a necessary prerequisite for Richardson extrapolation, is not reached, therefore values of $\Pi_{\text{ext}}$ could not be computed for free mesh. Extrapolated values of $\Pi$, corresponding to $h = 0$ (the theoretically infinitesimal mesh scale), are then plotted in Fig. 6.

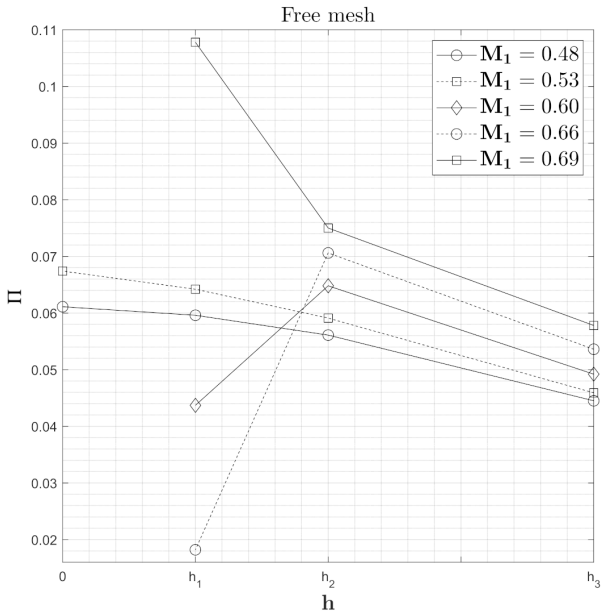


(a)

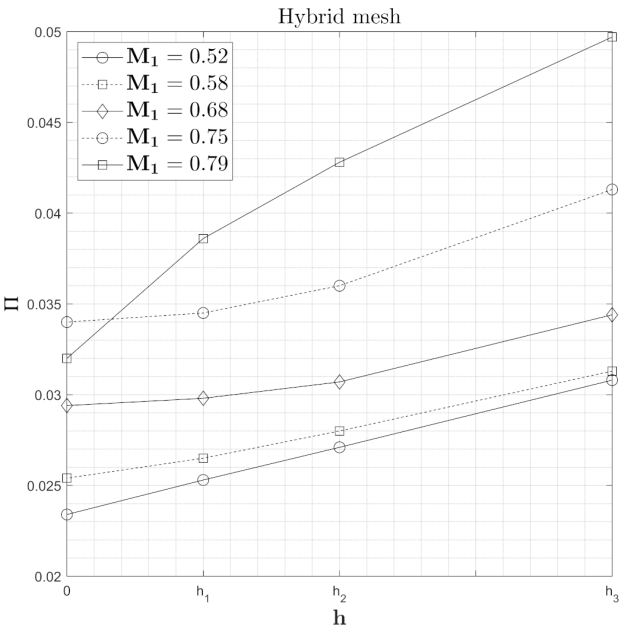


(b)

**Fig. 6.** Development of the total pressure loss coefficient depending on different meshes. (a) Free mesh; (b) Hybrid mesh

**Table 2**
Numerical results and Richardson extrapolation using different meshes

| Mesh type | Free | | | | |
|---|---|---|---|---|---|
| $M_1$ | 0.48 | 0.53 | 0.60 | 0.66 | 0.69 |
| $\Pi_3$ | 0.0445 | 0.0459 | 0.0492 | 0.0536 | 0.0578 |
| $\Pi_2$ | 0.0561 | 0.0591 | 0.0648 | 0.0706 | 0.0750 |
| $\Pi_1$ | 0.0596 | 0.0642 | 0.0437 | 0.0182 | 0.1078 |
| $n$ | 1.73 | 1.36 | × | × | × |
| $\Pi_{ext}$ | 0.0611 | 0.0674 | × | × | × |

| Mesh type | Hybrid | | | | |
|---|---|---|---|---|---|
| $M_1$ | 0.52 | 0.58 | 0.68 | 0.75 | 0.79 |
| $\Pi_3$ | 0.0308 | 0.0313 | 0.0344 | 0.0413 | 0.0459 |
| $\Pi_2$ | 0.0271 | 0.0280 | 0.0307 | 0.0360 | 0.0428 |
| $\Pi_1$ | 0.0253 | 0.0265 | 0.0298 | 0.0345 | 0.0386 |
| $n$ | 0.99 | 1.22 | 1.92 | 1.86 | 0.71 |
| $\Pi_{ext}$ | 0.0234 | 0.0254 | 0.0294 | 0.0340 | 0.0320 |

### 4.4. Grid convergence index

Suitable method to determine and report discretization errors estimates during simulations, which is firmly connected to Richardson extrapolation, is the grid convergence index. It allows the quantification of the uncertainty present due to mesh discretization by using two different meshes, original and refined. A band of probability around said solution can then be determined and although it is not explicitly an error bound, it gives a range of reliable chance of containing the accurate solution. [4] gives following equations

$$GCI_{32} = F_S \frac{|\epsilon_{32}|}{r^n - 1}, \qquad \epsilon_{32} = \frac{\Pi_3 - \Pi_2}{\Pi_2}, \tag{30}$$

$$GCI_{21} = F_S \frac{|\epsilon_{21}|}{r^n - 1}, \qquad \epsilon_{21} = \frac{\Pi_2 - \Pi_1}{\Pi_1}, \tag{31}$$

where $F_S$ is the factor of safety, $r$ is mesh refinement ratio and $n$ is the order of accuracy of the method. In our case, $F_S = 1.25$ is a recommended value for three meshes applied to a known problem according to [4]. Data obtained from simulations are stated in Table 3. Lastly, data from hybrid meshes are visualised in Fig. 7a, with confidence intervals determined by GCI method as

$$I = \langle \Pi_1(1 - GCI_{21}),\ \Pi_1(1 + GCI_{21}) \rangle.$$

GCI itself studied on medium and fine mesh ($GCI_{21}$) is shown in Fig. 7b, where rapid growth of the result uncertainty while

**Table 3**
Grid convergence index depending on different $M_1$ using different meshes

| Mesh type | Free | | | | |
|---|---|---|---|---|---|
| $M_1$ | 0.48 | 0.53 | 0.60 | 0.66 | 0.69 |
| $GCI_{32}$ | 0.111 | 0.177 | × | × | × |
| $GCI_{21}$ | 0.031 | 0.063 | × | × | × |

| Mesh type | Hybrid | | | | |
|---|---|---|---|---|---|
| $M_1$ | 0.52 | 0.58 | 0.68 | 0.75 | 0.79 |
| $GCI_{32}$ | 0.172 | 0.113 | 0.054 | 0.069 | 0.315 |
| $GCI_{21}$ | 0.093 | 0.051 | 0.015 | 0.020 | 0.213 |

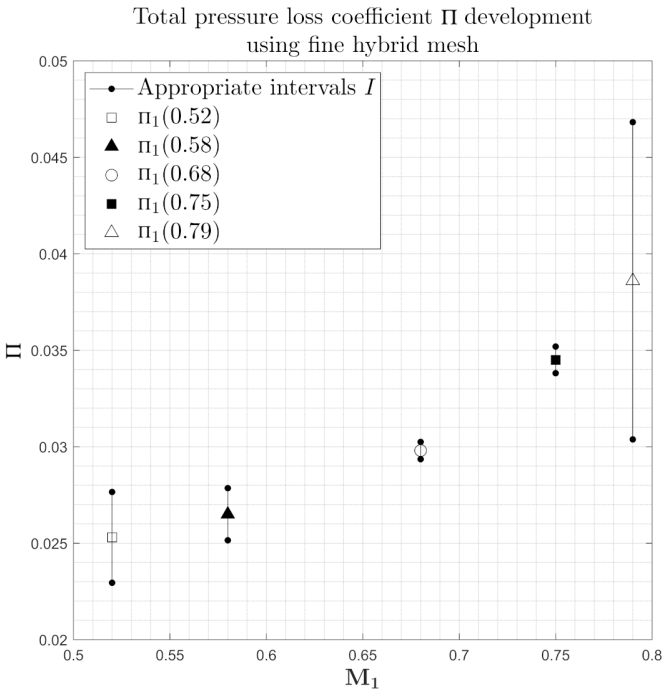


(a)

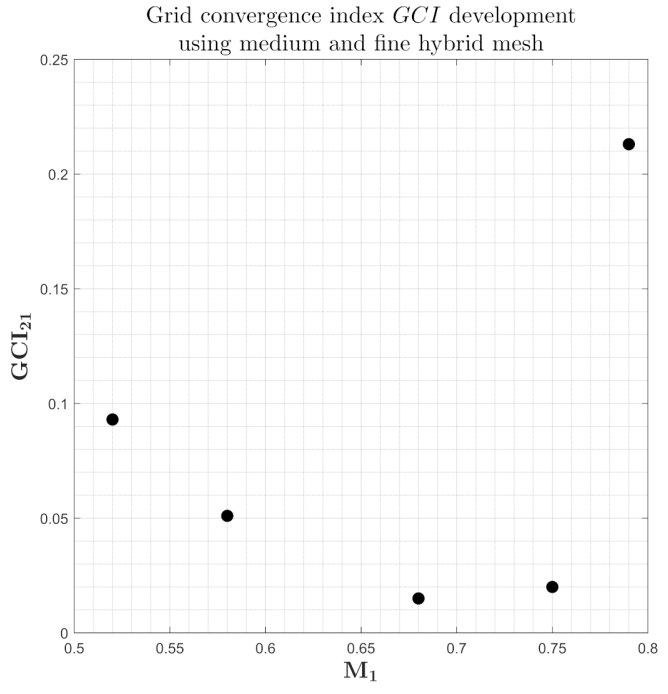


(b)

**Fig. 7.** GCI results. (a) Development of $\Pi_1$ with intervals $I$; (b) Development of $GCI_{21}$

approaching the cascade choking point can be seen, as well as light increase of uncertainty when decreasing the Mach number from the design point.

## 5. CONCLUSIONS

The CFD automation algorithm was presented and tested on well-known airfoil geometry described and investigated in [2]. This validation turned out quite well for negative and design angles of incidence. For positive angles, choking of the cascade occurs much later as Mach number rises. This phenomena is likely caused by axial velocity density ratio discussed in [20].

Thereafter, several simulations with test case geometry and design angle of incidence were performed and the results are listed in Table 2. Most of the free mesh results could not be interpreted in terms of the Richardson extrapolation and even if they could, there was a great deal of disagreement with results measured in [2]. This is considered to be due to poor capturing of the boundary layer.

The apparent order of the method approached the theoretical during hybrid mesh simulations as the inlet Mach number was close to the design one. Using data from Richardson extrapolation, investigation of GCI was performed. Accuracy decrease was observed as Mach number decreased from the design conditions, but more importantly rapid increase in inaccuracy occurs while getting closer to choking point, which could in turn be connected with increasing Reynolds number and could be solved by further refinement of mesh at wall boundaries. Results from Richardson extrapolation and GCI investigation performed on hybrid meshes were visualized in the last section.

In conclusion, free mesh failed this suitability test greatly, gives untrustworthy results and therefore should not be used for this kind of problem. On the other hand, hybrid mesh confirmed itself as a sufficient meshing strategy which gives accurate results around design conditions.

Further work will concern the analysis of fully structured meshes. Thereafter, this automation tool will be merged with optimization algorithm and airfoil generator, resulting in powerful design tool for ideal airfoil shapes. Finally, this optimization tool will be paired with simple axial compressor design algorithm from [21] and with a program that composes compressor blading introduced in [22].

## ACKNOWLEDGEMENTS

Authors acknowledge support from the ESIF, EU Operational Programme Research, Development and Education, and from the Center of Advanced Aerospace Technology (CZ.02.1.01/0.0/0.0/16 019/0000826), Faculty of Mechanical Engineering, Czech Technical University in Prague.

## REFERENCES

[1] S. Farokhi, *Aircraft Propulsion*. United Kingdom: John Wiley & Sons, 2014.

[2] W. Steinert, B. Eisenberg, and H. Starken, "Design and testing of a controlled diffusion airfoil cascade for industrial axial flow compressor application," in *Proceedings of the ASME 1990 International Gas Turbine and Aeroengine Congress and Exposition.*, ser. Turbo Expo: Power for Land, Sea, and Air, vol. 1: Turbomachinery, Brussels, Belgium, 1990, p V001T01A044, doi: 10.1115/1.2929119.

[3] P. Zachos, N. Grech, B. Charnley, V. Pachidis, and R. Singh, "Experimental and numerical investigation of a compressor cascade at highly negative incidence," *Eng. Appl. Comp. Fluid Mech.*, vol. 5, no. 1, pp. 26–26, 2011, doi: 10.1080/19942060.2011.11015350.

[4] P. Roache, *Verification and Validation in Computational Science and Engineering*. Albuquerque, New Mexico: Hermosa Publishers, 1998.

[5] V. Carrillo, J. Petrie, and E. Pacheco, "Application of the grid convergence index to a laminar axisymmetric sudden expansion flow," *Mascana*, vol. 5, pp. 115–123, 2016.

[6] I. Celik and O. Karatekin, "Numerical experiments on application of richardson extrapolation with nonuniform grids," *ASME J. Fluids Eng.*, vol. 119, no. 3, pp. 584–590, 1997, doi: 10.1115/1.2819284.

[7] A. Meana-Fernández, J. Oro, K. Argüelles Díaz, M. Galdo-Vega, and S. Velarde-Suárez, "Application of richardson extrapolation method to the cfd simulation of vertical-axis wind turbines and analysis of the flow field," *Eng. Appl. Comp. Fluid Mech.*, vol. 13, no. 1, pp. 359–376, 2019, doi: 10.1080/19942060.2019.1596160.

[8] L. Kwaśniewski, "Application of grid convergence index in fe computation," *Bull. Pol. Acad. Sci. Tech. Sci.*, vol. 61, no. 1, pp. 123–128, 2013, doi: 10.2478/bpasts-2013-0010.

[9] S. Hirsch, *Numerical computation of internal and external flows*. Amsterdam: Elsevier, 2007.

[10] M. Landahl and E. Mollo-Christensen, *Turbulence and Random Processes in Fluid Mechanics*. Cambridge: Cambridge University Press, 1992.

[11] T. Gatski and J.-P. Bonnet, *Compressibility, Turbulence and High Speed Flow*. Amsterdam: Elsevier, 2009.

[12] D. Wilcox, *Turbulence Modeling for CFD*. Canada, CA: DCW Industries, 2006.

[13] R. Langtry and F. Menter, "Correlation-based transition modeling for unstructured parallelized computational fluid dynamics codes," *AIAA J.*, vol. 47, no. 12, pp. 2894–2906, 2009, doi: 10.2514/1.42362.

[14] F. Menter, "Two-equation eddy-viscosity turbulence models for engineering applications," *AIAA J.*, vol. 32, no. 8, pp. 1598–1605, 1994, doi: 10.2514/3.12149.

[15] J. Holman and J. Fürst, "Numerical simulation of separation induced laminar to turbulent transition over an airfoil," *J. Comput. Appl. Math.*, vol. 394, p. 113530, 2021, doi: 10.1016/j.cam.2021.113530.

[16] J. Blazek, *Computational Fluid Dynamics: Principles and Applications*. Amsterdam: Elsevier, 2015.

[17] S. Acharya, B. Baliga, K. Karki, J. Murthy, C. Prakash, and S. Vanka, "Pressure-based finite-volume methods in computational fluid dynamics," *ASME. J. Heat Transf.*, vol. 129, no. 4, pp. 407–424, 2007, doi: 10.1115/1.2716419.

[18] M. Darwish and F. Moukalled, "A fully coupled navier-stokes solver for fluid flow at all speeds," *Numer. Heat Tranf. Part B-Fundam.*, vol. 65, no. 5, pp. 410–444, 2014, doi: 10.1080/10407790.2013.869102.

[19] Z. Zlatev and I. Dimov, *Richardson Extrapolation*. Berlin: De Gruyter, 2018.

[20] R. Kumaran, S. Kamble, K. Swamy, Q. Nagpurwala, and A. Bhat, "Effect of axial velocity density ratio on the performance of a controlled diffusion airfoil compressor cascade," *Int. J. Turbo. Jet-Engines*, vol. 32, no. 4, pp. 305–317, 2015, doi: 10.1515/tjj-2014-0036.

[21] J. Ruzek and P. Kmoch, *Theory of Aircraft Engines – Part I: Compressors, Turbines and Combustion Chambers (Teorie Leteckých Motorů – Část I: Kompresory, Turbíny a Spalovací Komory)*. Brno: Vojenská akademie Antonína Zápotockého, 1979.

[22] J. Crouse, D. Janetzke, and R. Schwirian, *A Computer Program for Composing Compressor Blading from Simulated Circular-Arc Elements on Conical Surfaces*. NASA, 1969.